1 Evidence of warm and humid interstadials in central Europe during early MIS 3

2 revealed by a multi-proxy speleothem record

3

4 Michael Weber[1,2]*, Denis Scholz[1], Andrea Schröder-Ritzrau[3], Michael Deininger[1], Christoph

5 Spötl[4], Federico Lugli[5,6], Regina Mertz-Kraus[1], Klaus Peter Jochum[2], Jens Fohlmeister[7,8],

6 Cintia F. Stumpf[9], Dana F.C. Riechelmann[1]

7

8 [1]Institute of Geosciences, Johannes Gutenberg-University Mainz, Johann-Joachim-Becher-

9 Weg 21, 55128 Mainz, Germany

10 [2]Climate Geochemistry Department, Max Planck Institute for Chemistry (Otto-Hahn-Institute),

11 Postbox 3060, 55020 Mainz, Germany

12 [3]Institute for Environmental Physics, University Heidelberg, Im Neuenheimer Feld 229,

13 69120 Heidelberg, Germany

14 [4]Institute of Geology, University of Innsbruck, Innrain 52, 6020 Innsbruck, Austria

15 [5]Department of Chemical and Geological Sciences, University of Modena and Reggio Emilia,

16 Via Campi 103, 41125, Modena, Italy

17 [6]Department of Cultural Heritage, University of Bologna, 48121 Ravenna, Italy

18 [7]Institute for Earth and Environmental Sciences, University of Potsdam, Karl-Liebknecht-Str.

19 24-25, 14476 Potsdam-Golm, Germany

20 [8]GFZ German Research Centre for Geosciences, Section 5.2 Climate Dynamics and Landscape

21 Development, Telegrafenberg, 14473 Potsdam, Germany

22 [9]Universidade de Brasília, Instituto de Geociências, 70294-400 Brasília, Brazil

23

24 *Corresponding author:

25 Michael Weber

26   Institute of Geosciences, Johannes Gutenberg University Mainz, Johann-Joachim-Becher-

27   Weg 21, 55128 Mainz, Germany

28   Email: mweber02@students.uni-mainz.de

29

30 **Abstract**

31 Marine Isotope Stage 3 (MIS 3, 57 – 27 ka) was characterised by numerous rapid climate

32 oscillations (i.e., Dansgaard-Oeschger (D/O-) events), which are reflected in various climate

33 archives. So far, MIS 3 speleothem records from central Europe have mainly been restricted to

34 caves located beneath temperate Alpine glaciers or close to the Atlantic Ocean. Thus, MIS 3

35 seemed to be too cold and dry to enable speleothem growth north of the Alps in central Europe.

36 Here we present a new speleothem record from Bunker Cave, Germany, which shows two

37 distinct growth phases from 52.0 (+0.8, -0.5) to 50.9 (+0.6, -1.3) ka and 47.3 (+1.0, -0.6) to

38 42.8 (± 0.9) ka, rejecting this hypothesis. These two growth phases potentially correspond to

39 the two warmest and most humid phases in central Europe during MIS 3, which is confirmed

40 by pollen data from the nearby Eifel. The hiatus separating the two phases is associated with

41 Heinrich stadial 5 (HS 5), although the growth stop precedes the onset of HS 5. The first growth

42 phase is characterised by a fast growth rate, and Mg concentrations and Sr isotope data suggest

43 high infiltration and the presence of soil cover above the cave. The second growth phase was

44 characterised by drier, but still favourable conditions for speleothem growth. During this phase,

45 the $\delta^{13}C$ values show a significant decrease associated with D/O-event 12. The timing of this

46 shift is in agreement with other MIS 3 speleothem data from Europe and Greenland ice core

47 data.

1. Introduction

Marine Isotope Stage 3 (MIS 3, ca. 57-27 ka; Lisiecki and Raymo, 2005) was characterised by rapid climate oscillations (i.e., the Dansgaard-Oeschger (D/O) events). This high-frequency climate variability was first discovered in Greenland ice cores by Johnsen et al. (1992) and Dansgaard et al. (1993). Stable oxygen isotope (δ^{18}O) records obtained from ice cores show the occurrence of high-magnitude climate cycles, where a rapid temperature increase (up to 10 to 16 °C on the summit of Greenland, Huber et al., 2006; Kindler et al., 2014) occurred within decades and was followed by a gradual cooling. For MIS 3, eleven D/O-events have been described in Greenland ice cores (D/O 5 – 15), based on the GICC05 timescale (Rasmussen et al., 2014). Furthermore, MIS 3 was characterised by Heinrich events 3 to 5, triggered by freshwater input in the North Atlantic, slowing down North-Atlantic deep-water formation (Böhm et al., 2015) and identified by ice-rafted debris (IRD) layers (Heinrich, 1988). The corresponding Heinrich stadials were cold phases with a typical duration of few thousand years, identified both in Greenland ice cores and in North Atlantic and Mediterranean sediment cores (e.g., Bond et al., 1993; Cacho et al., 1999; Sánchez Goñi et al., 2002). These marine records, however, often lack independent and precise dating control, rendering the identification of leads and lags during D/O-events partly ambiguous.

Speleothems have been used as archives of past climate and environmental variability in Europe (e.g., Fankhauser et al., 2016; Fohlmeister et al., 2012; Genty et al., 2003; Luetscher et al., 2015). The U-series disequilibrium method (Richards and Dorale, 2003; Scholz and Hoffmann, 2008) allows to obtain accurate and precise age-depth models. In addition, stable carbon and oxygen isotopes as well as trace elements can be measured at high temporal resolution in speleothems and have been widely used to investigate past climate change (Fairchild et al., 2006; Fairchild and Treble, 2009; Lachniet, 2009; McDermott, 2004). Furthermore, speleothem growth itself can be used as climate proxy, especially during glacial periods. Speleothem

75　growth depends on several climatic and environmental factors, such as the availability of water

76　(i.e., temperature $> 0 \, ^{\circ}C$) and a high pCO_2 in the soil above the cave (Mattey et al., 2016).

77　Consequently, speleothem growth is mainly restricted to relatively warm and humid climate

78　periods that are characterised by the availability of water, sufficient soil development and

79　vegetation cover above the cave, such as during the Holocene (Mangini et al., 2007; McDermott

80　et al., 1999) and previous interglacials (Baker et al., 1993; Gordon et al., 1989; Hennig et al.,

81　1983). This results in drip water supersaturated with respect to calcite entering the cave and,

82　eventually, the precipitation of speleothem calcite.

83　European speleothem records from MIS 3 are limited. Besides some records from southern and

84　south-eastern Europe with only single ages indicating growth during MIS 3 (Constantin et al.,

85　2007; Hodge et al., 2008), the majority of MIS 3 speleothem records have so far been reported

86　from the Alpine region (Holzkämper et al., 2005; Luetscher et al., 2015; Moseley et al., 2014;

87　Spötl and Mangini, 2002; Spötl et al., 2006). These speleothems grew in caves underneath

88　temperate glaciers, which provided enough meltwater to enable speleothem growth (Spötl and

89　Mangini, 2002), despite of cold climate conditions at the surface. Therefore, their growth cannot

90　be used as a direct climate indicator, in particular for central Europe. Further speleothems from

91　MIS 3 have been found in south-western (SW) and north-eastern (NE) France. In particular,

92　MIS 3 stalagmites from Villars Cave (SW France) were subject of several studies and provided

93　valuable information about climate variability during this period (Genty et al., 2003; Genty et

94　al., 2005; Genty et al., 2010; Wainer et al., 2009). Another MIS 3 speleothem was found at

95　Grotte des Puits de Pierre-la-Treiche (NE France, Pons-Branchu et al., 2010). The most north-

96　western European MIS 3 speleothem record was published from Crag Cave (SW Ireland),

97　where several broken stalagmites have been dated (Fankhauser et al., 2016). These authors

98　showed that speleothem growth occurred episodically during MIS 3 interstadials, especially

99　during mid to late MIS 3.

100   Here we present a new record of a stalagmite from Bunker Cave, central Germany, which grew

101   during MIS 3. Currently, this is the northern-most MIS 3 speleothem record for central Europe,

102   where centennial-scale climate records of this time interval are rare (McDermott, 2004;

103   Voelker, 2002). The record shows two warm and humid phases during early MIS 3 separated

104   by a hiatus corresponding to the Heinrich 5 cold event (HS 5).

105

106   **2. Site and sample description**

107   2.1. Bunker Cave

108   Bunker Cave has been described in detail by Riechelmann et al. (2011) and Fohlmeister et al.

109   (2012) and is thus only briefly discussed here. The cave (51°22'03''N, 7°39'53''E) is located

110   in western Germany (Sauerland, Fig. 1), the cave entrance at 184 m above sea level. The cave

111   is developed in Middle to Upper Devonian low-Mg limestone, which contains dolomite veins,

112   and the limestone overburden ranges from 15 to 30 m (Grebe, 1993). At present, the host rock

113   is covered by up to 70 cm of brownish loamy soil, which developed from loess loam deposited

114   during the last glacial (von Kamp and Ribbert, 2005). The thin soil horizon A (<10 cm) is

115   humic, covering a brown/yellow soil horizon B. Soil horizon C is built up by this brown/yellow

116   soil and the limestone host rock (Riechelmann et al., 2011). Today, the vegetation above the

117   cave consists of C3-plants, mainly ash and beech trees as well as shrubs. The mean annual cave

118   air and drip water temperature is 10.6°C (2006 – 2009). Mean annual precipitation in the area

119   is 919 mm (1988 – 2007, weather station Hagen-Fley), equally distributed over the year. The

120    $\delta^{18}O$ values of precipitation range from -5 ‰ in summer to -13 ‰ in winter (Riechelmann et

121   al., 2017). The $\delta^{18}O$ values of cave drip water (mean $\delta^{18}O$ = -7.9 ± 0.3 ‰, 1σ SD, n = 384, 2006

122   – 2013, Riechelmann et al., 2017) imply a well-mixed aquifer. Calcite precipitation in Bunker

123   Cave was observed during the whole year by watch glass experiments at several drip sites (mean

124    $\delta^{13}C$ = -8.6 ± 0.6 ‰, 1σ SD, n = 16; mean $\delta^{18}O$ = -6.1 ± 0.2 ‰, 1σ SD, n = 16, Riechelmann,

125   2010; Riechelmann et al., 2014). Therefore, Bunker Cave is highly suitable for reconstruction

126   of long-term multi-annual climate trends in central Europe (Fohlmeister et al., 2012;

127   Riechelmann et al., 2011; Riechelmann et al., 2012b; Riechelmann et al., 2017).

128
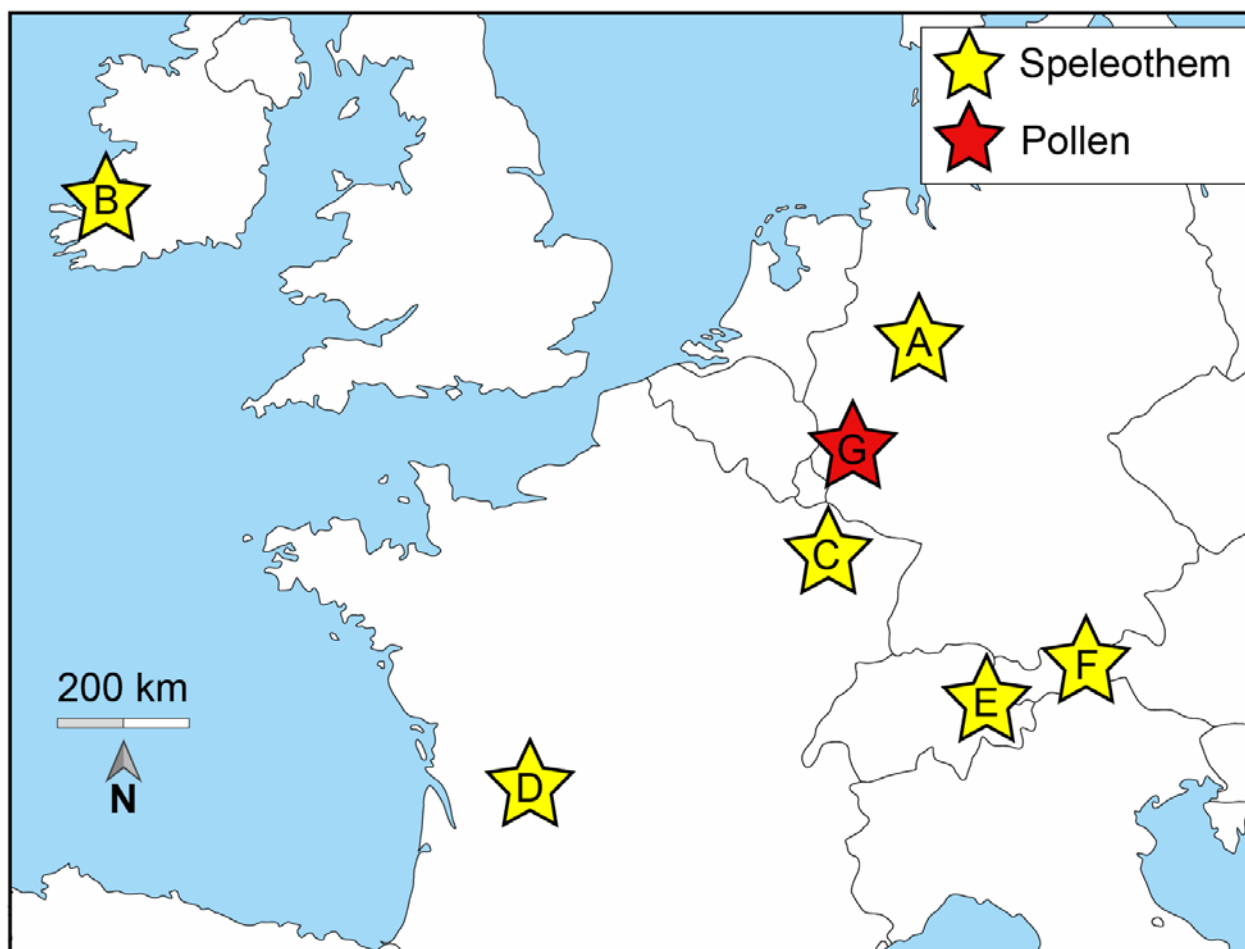
Fig.1: Map showing north-western parts of Europe with the location of MIS 3 climate records from Bunker Cave [A, this study], Crag Cave [B, Fankhauser et al. (2016)], Grotte des Puits de Pierra-la-Treiche [C, Pons-Branchu et al. (2010)], Villars Cave [D, Genty et al. (2003)], Hölloch Cave [E, Moseley et al. (2014)], Kleegruben Cave [F, Spötl et al. (2006)] and the Eifel maar lakes [G, Sirocko et al. (2016)].

2.2. Stalagmite Bu2

Bu2 (Fig. 2) is a 32 cm-long stalagmite, sampled under an active drip site, which was investigated in the framework of a long-term cave monitoring program (corresponding to drip site TS 7, Riechelmann et al., 2011). The upper 76 mm of Bu2 grew during the Holocene and were already studied by Fohlmeister et al. (2012). Bu2 consists of clear white to beige calcite with only few detrital layers (Fig. 2). A single brown layer at 76 mm distance from top (DFT), separating the Holocene growth phase from the older part of Bu2, is clearly visible. The base of the stalagmite (Fig. 2) consists of brownish calcite and was not analysed.

140
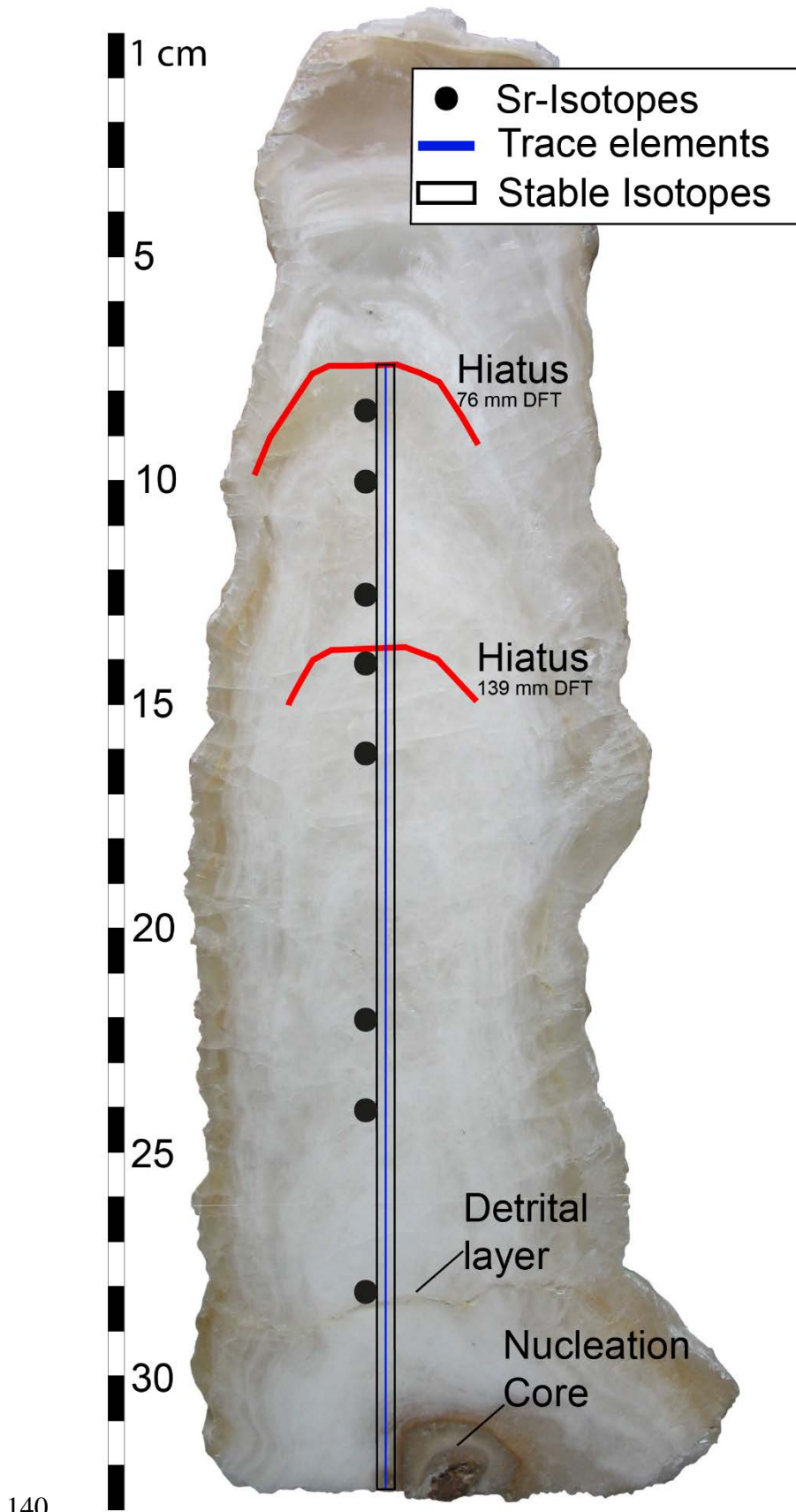
Fig. 2: Slab of speleothem Bu2 showing petrographic features and sampling details. Sample

locations for ^{230Th}/U-dating are presented in supplementary Table A1.

143

3. Methods

3.1. ^{230}Th/U-dating

In total, 25 samples were cut along the growth axis of Bu2 using a diamond wire saw. The samples were subsequently prepared for ^{230}Th/U-dating by multi-collector inductively coupled plasma mass spectrometry (MC-ICP-MS, 23 samples) and thermal ionisation mass spectrometry (TIMS, 2 samples). The TIMS analyses were performed at the Heidelberg Academy of Sciences, following the methods described by Scholz et al. (2004), using an updated spike re-calibration (Hoffmann et al., 2007). For the MC-ICP-MS analyses, sample amounts of approximately 0.3 g were used. After sawing, the samples were briefly leached in weak HNO_3 to remove potential surface contamination. The chemical separation of U and Th was performed as described by Hoffmann (2008) with the respective adjustments described by Yang et al. (2015). Uranium and Th fractions were measured separately, using a Nu plasma MC-ICP-MS at the Max Planck Institute for Chemistry (MPIC) in Mainz. A standard-bracketing approach was applied to correct for mass fractionation, ion counter gain and tailing. The mass spectrometric procedures were generally explained in Hoffmann et al. (2007) and in detail for the laboratory at the MPIC by Obert et al. (2016). The calibration of the U-Th-spike was described in detail by Gibert et al. (2016). Introduction of the sample solution was performed using a CETAC Aridus II desolvating nebulizer system, connected to the MC-ICP-MS. Daily tuning (including torch position, gas flows and ion lenses) was performed to obtain highest signal intensities at optimized peak shapes. Resulting ages were then used for the calculation of the age-depth relationship (Fig. 3), using the algorithm StalAge (Scholz and Hoffmann, 2011). Further details are summarised in supplementary Table A1.

166

167 3.2. Trace element analysis

168 Trace element concentrations were determined by laser ablation inductively coupled plasma

169 mass spectrometry (LA-ICP-MS). The upper 98 mm of the sample were analysed at the Goethe

170 University Frankfurt, using a New Wave UP213 UV-laser system, connected to a Thermo-

171 Finnigan Element II SF-ICP-MS (Gerdes and Zeh, 2006). For the measurements between 98

172 and 324 mm DFT, an ArF Excimer 193 nm laser system (ESI NWR193), coupled to an Agilent

173 7500ce ICP-MS at the Johannes Gutenberg University Mainz, was used (Jochum et al., 2012).

174

175 Prior to both LA-ICP-MS analyses, the signal was tuned for maximum intensities at low oxide

176 formation rates measured as $^{238}U^{16}O/^{238}U$ <0.2 % (Mainz) and <0.5 % (Frankfurt). Ion

177 intensities for ^{25}Mg, ^{43}Ca, ^{88}Sr and ^{89}Y were continuously acquired parallel to the growth axis,

178 located within 2 mm distance of the stable isotope track (Fig. 2). Prior to each analysis, a pre-

179 ablation was performed. Background counts were measured for 15 s without the laser firing

180 before each analysis and subtracted from the raw data. The transect was divided into

181 consecutive lines of approximately 4 cm length, allowing to analyse NIST SRM 610 (Frankfurt)

182 and NIST SRM 612 (Mainz) at the beginning, between each line and at the end of the routine

183 for calibration purposes. To monitor accuracy and reproducibility, NIST SRM 610 (n =24),

184 USGS MACS-3 (n = 24) and USGS BCR-2G (n = 24) were monitored as unknowns during the

185 analyses at the Johannes Gutenberg University Mainz (see supplementary Table A2). Data

186 reduction was performed using an in-house Excel spreadsheet. Details of the calculations are

187 given in Mischel et al. (2017).

188 ^{43}Ca was used as an internal standard, applying the corresponding Ca concentration from the

189 GeoReM database (Jochum et al., 2005). For the stalagmite sample, a Ca-content of 39.4 wt%

190 was assumed. Reference values for NIST SRM 610 and 612 were adapted from Jochum et al.

191 (2011). Further operational parameters are given in supplementary Table A3.

192

193 3.3. Stable isotope analysis

194 High-resolution stable carbon and oxygen isotopes values ($\delta^{13}C$ and $\delta^{18}O$) were obtained at the

195 Institute of Geology, University of Innsbruck. In total, 1078 samples were drilled using a

196 Merchantek video-controlled MicroMill device with a spatial resolution of 150 µm in the upper

197 part of Bu2 (between 76 and 141.75 mm DFT) and 300 µm in the lower part of Bu2 (between

198 142 and 324 mm DFT, Fig. 2). The $\delta^{13}C$ and $\delta^{18}O$ analyses were performed using a Thermo

199 Fisher Delta^{plus}XL isotope ratio mass spectrometer linked to a Gasbench II. Analytical precision

200 for the $\delta^{13}C$ and $\delta^{18}O$ measurements is 0.07 ‰ for $\delta^{13}C$ and 0.09 ‰ for $\delta^{18}O$ (both at the

201 1σ level). All $\delta^{13}C$ and $\delta^{18}O$ values are reported relative to V-PDB.

202 To account for changes in seawater $\delta^{18}O$ values due to changing sea level and ice volume, we

203 applied the correction factor of Duplessy et al. (2007) assuming a decrease of -0.008 ± 0.002 ‰

204 per meter of global sea-level rise and using the sea-level reconstruction of Bates et al. (2014b),

205 which is based on the composite ODP record 162-980/981 (Bates et al., 2014a). The effect of

206 the correction on the $\delta^{18}O_{slc}$ (slc = sea-level corrected) values of Bu2 is +0.56 ‰ between 76

207 and 139.3 mm DFT and +0.63 ‰ between 139.3 and 324 mm DFT. Thus, the difference

208 between these two sections is only 0.07 ‰, which is comparable with the analytical uncertainty

209 of the $\delta^{18}O$ measurements. The effect of the sea-level correction is shown in supplementary

210 Fig A1.

211

212 3.4. Sr-isotope analysis

213 $^{87}Sr/^{86}Sr$ ratios were determined for Bu2 as well as for several other samples from the cave

214 environment (i.e., soil and host rock). The samples of Bu2 (20 to 30 mg) were processed and

215 analysed using a Neptune MC-ICP-MS at the Laboratory of Isotope Geochemistry of the

216   Department of Chemical and Geological Sciences, University of Modena and Reggio Emilia,

217   Italy, following the methods described by Lugli et al. (2017) and Weber et al. (2018) for

218   dissolution analyses and separation of Sr from matrix elements.

219   Seven Faraday detectors were used to measure the ion beams of the following masses

220   simultaneously: ^{82}Kr, ^{83}Kr, ^{84}Sr, ^{85}Rb, ^{86}Sr, ^{87}Sr, ^{88}Sr. Strontium solutions were diluted to

221   ~0.25 mg/l and introduced into the mass spectrometer via a quartz spray chamber and a

222   nebulizer with an uptake rate of 100 µl/min. Samples were analysed, together with standard and

223   blank solutions, in a static-multi-collection mode with single blocks of 100 cycles (integration

224   time 8.4 s per cycle). A bracketing sequence was employed to correct for instrumental drifts.

225   Krypton in the Ar gas was monitored and corrected using a ^{86}Kr/^{83}Kr ratio of 1.505657 and

226   background subtraction. To correct for the presence of isobaric Rb on mass 87, a ^{87}Rb/^{85}Rb

227   ratio of 0.3856656 was used. Mass bias correction was performed using an exponential law and

228   a stable ^{88}Sr/^{86}Sr ratio of 8.375209. Strontium ratios were corrected using the NIST SRM

229   987 ^{87}Sr/^{86}Sr ratio of 0.710248 (McArthur et al., 2001). Daily repeated measurements of the

230   NIST SRM 987 yielded a mean ^{87}Sr/^{86}Sr ratio of 0.710241 ± 0.000012 (2σ; n = 20).

231   ^{87}Sr/^{86}Sr ratios of host rock and soil samples from Bunker Cave were measured by TIMS at the

232   Institute of Environmental Physics, Heidelberg University. Strontium separation was performed

233   using Sr spec™ ion exchange resin columns. The sample size was chosen according to the Sr

234   concentration providing approximately 100 ng of Sr on the filament and assuming 100%

235   chemical yield. Soil samples were quantitatively extracted using HF. Column chemistry was

236   performed two times using supra pure acids in order to receive sufficient chemical separation

237   from CaCO$_3$. The eluate was reduced to 2 µl and transferred onto a Re filament. Subsequent

238   measurements (10 sequences á 10 measurements) were performed using a Finnigan MAT 262

239   in multi-dynamic mode. All isotopes were measured on Faraday cups with minimum ^{86}Sr

240   intensities of 0.5 V. Each measurement was checked for ^{85}Rb. Isotope ratios were corrected for

241   internal mass fractionation assuming a stable $^{88}Sr/^{86}Sr$ ratio of 8.375209. Repeated

242   measurements of NIST SRM 987 yielded $^{87}Sr/^{86}Sr = 0.710266 \pm 0.000010$ (2σ; n = 14).

243

244   **4. Results**

245   4.1. $^{230}Th/U$-dating

246   Results of $^{230}Th/U$-dating are presented in supplementary Table 1. In addition to the previously

247   published Holocene part of Bu2 (Fohlmeister et al., 2012), dating revealed two distinct growth

248   phases during early MIS 3. Based on the age model, the first growth phase (in the following

249   referred to as MIS 3 phase 1) started at 52.0 (+0.8, -0.5) ka and ended at 50.9 (+0.6, -1.3) ka.

250   The second growth phase (in the following referred to as MIS 3 phase 2) began at 47.3 (+1.0, -

251   0.6) ka and ended at 42.8 (± 0.9) ka. The growth rates calculated based on the age-depth model

252   are remarkably different between the two growth phases (supplementary Fig. A2). MIS 3

253   phase 1 is characterised by an exceptionally fast growth rate of 120 – 390 µm/a, which

254   decreases to ~40 – 60 µm/a at approximately 170 mm DFT. MIS 3 phase 2 starts with an

255   average growth rate of ~25 µm/a, which further decreases to ~8 µm/a at approximately 100 mm

256   DFT.

257   In general, the ^{232}Th and ^{238}U concentrations decrease with increasing age (supplementary

258   Table 1). The $(^{230}Th/^{232}Th)$ activity ratio, an indicator for the degree of detrital contamination,

259   changes between the two growth phases. MIS 3 phase 1 shows generally higher $(^{230}Th/^{232}Th)$

260   activity ratios between ~1000 and 5100 (mean = 2335 ± 1125, 1 SD; besides sample Bu2-29),

261   while MIS 3 phase 2 shows ratios between ~150 and 840 (mean = 371 ± 212, 1σ SD). Detrital

262   correction does not have a significant influence on the ^{230}Th-ages (supplementary Table 1). An

263   unsuccessful dating attempt at 291.5 mm DFT (Bu2-29), which included parts of the detrital

264   layer, yielded an age of ~45 ka instead of an expected age of ~51 ka, which indicates that this

265 layer is possibly influenced by post-depositional U-addition (Bajo et al., 2016; Scholz et al.,

266 2014).

267 We note that there is a step in the age model of Bu2 between 98 and 101 mm DFT (Fig. 3). To

268 evaluate the possibility of a hiatus at this depth, thin sections (supplementary Figs. A4 and A5)

269 and trace elements were analysed. As none of these analyses showed evidence of a growth

270 interruption, the age model was constructed without including a hiatus resulting in a slow

271 growth rate between these two data points of approximately 5 μm/a.

272
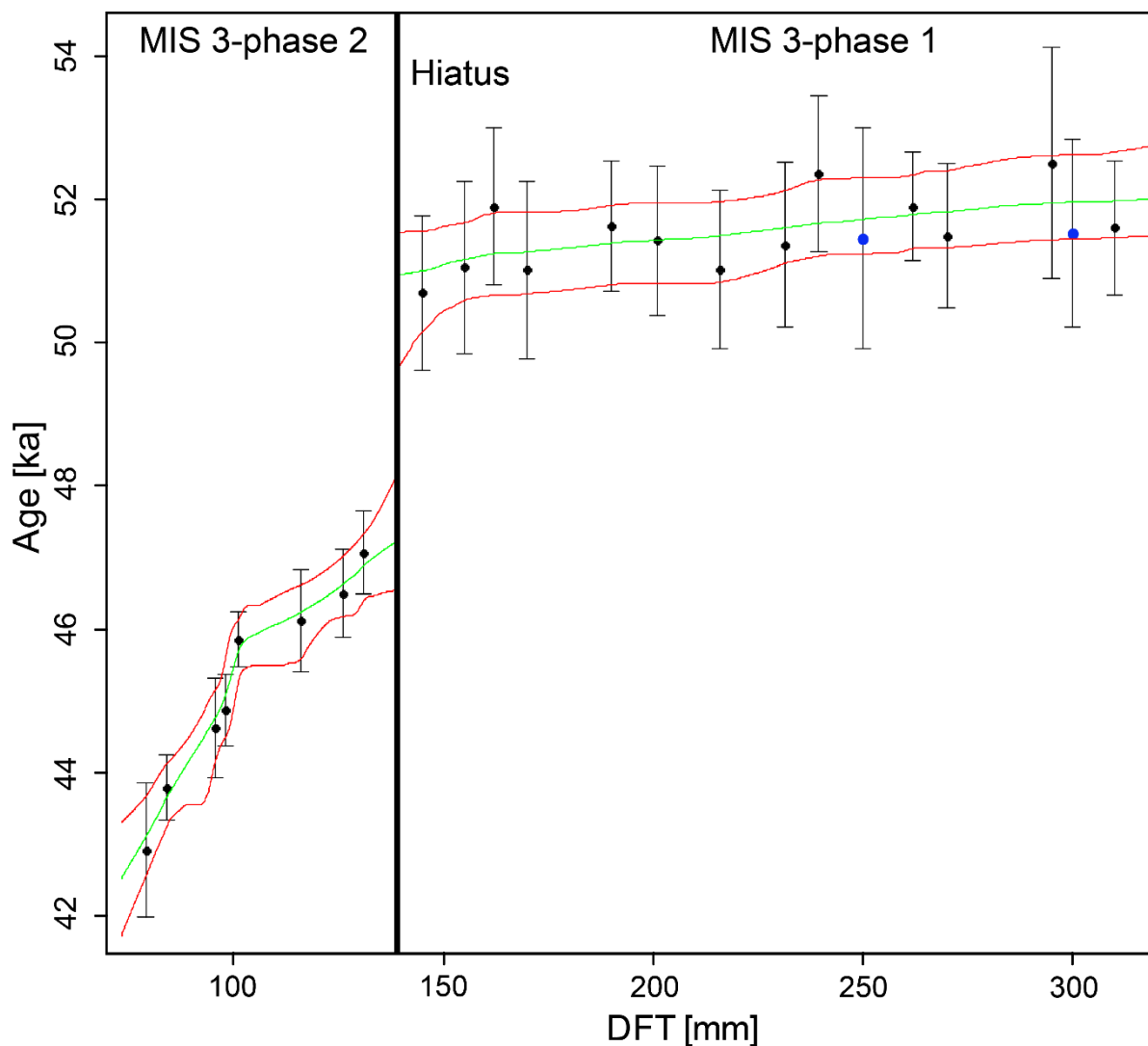
273

274 **Fig. 3:** Age-depth relationship for stalagmite Bu2. Black points show the MC-ICP-MS ^{230}Th-

275 ages, blue points highlight the two ages measured by TIMS (supplementary Table A1). The

276   green line represents the age model calculated by StalAge (Scholz and Hoffmann, 2011), while

277   red lines show the corresponding age-uncertainties (95% confidence interval). The vertical

278   black line marks the hiatus between the two growth phases and was guided by the abrupt change

279   in Y concentration (see section 4.2).

280

281   4.2. Trace elements and stable isotopes

282   The trace element records of Mg, Sr and Y as well as the stable isotope values are shown in

283   Fig. 4. The trace element data were averaged by a 25 point-running mean.

284
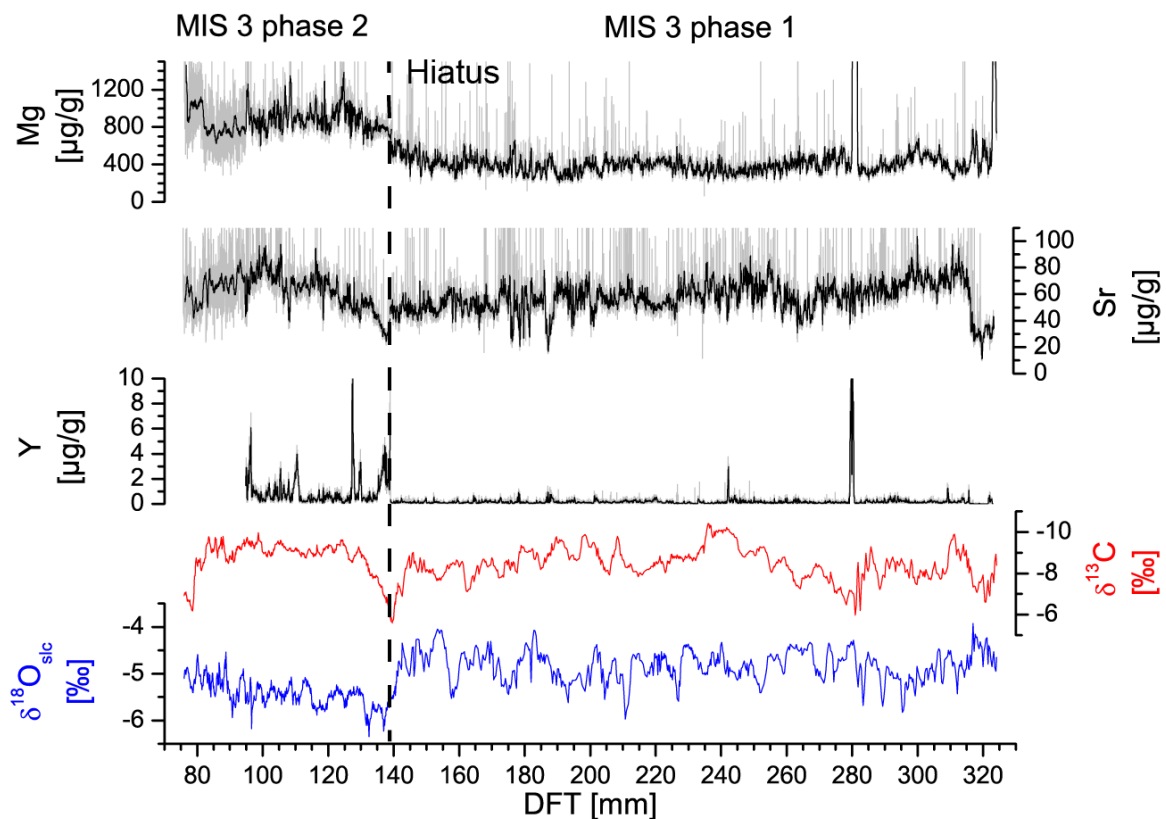
285

286   **Fig. 4:** Concentrations of Mg, Sr and Y (high resolution data shown by grey lines) as well as

287     $\delta^{18}O_{slc}$ (blue) and $\delta^{13}C$ (red) values of speleothem Bu2 shown versus distance from top (DFT).

288 Note that the δ^{13}C axis is inverted. A hiatus was identified at 139.3 mm DFT. The spike in Mg

289 and Y at 280 – 282 mm DFT is due to a detrital layer (see Fig. 2).

290

291 At 76.3 mm DFT, a rather high Mg concentration is visible. This corresponds to the growth

292 stop between MIS 3 and the Holocene and is in agreement with the dating results showing the

293 oldest Holocene age at 75 mm DFT and the youngest MIS 3 age at 79 mm DFT. Furthermore,

294 the stalagmite shows a prominent brownish layer at this depth (Fig. 2). The boundary within

295 the MIS 3 growth phase between approximately 47 and 51 ka (Fig. 3) can be also recognised in

296 the trace element data. Based on the dating results, this hiatus is located between 145 and

297 131 mm DFT (Fig. 3). The concentration of the different trace elements changes between the

298 two MIS 3 growth phases. Yttrium shows a significant peak of up to 7 µg/g at 139.3 mm DFT,

299 which is much higher than the usual background value of <<1 µg/g. At the same DFT, Mg

300 shows a gradual increase from ~500 µg/g up to ~800 µg/g (Fig. 4). The Mg concentration

301 ranges between 300 and 400 µg/g for MIS 3 phase 1 and shows higher concentrations during

302 MIS 3 phase 2, ranging from 800 to 1000 µg/g. This is robust evidence for the location of the

303 hiatus at ~139.3 mm DFT.

304 Magnesium and Y show a rapid increase at 280 – 282 mm DFT (Fig. 4), which corresponds to

305 a layer of brownish calcite (Fig. 2). This increase is probably related to detrital material.

306 Although we cannot exclude a short hiatus associated with this detrital layer, our age model

307 cannot resolve it. Thus, we assume continuous growth during MIS 3 phase 1.

308 Strontium concentrations vary between 40 and 90 µg/g. During MIS 3 phase 1, Sr shows a

309 significant increase (20 up to 80 µg/g) at the beginning of the record followed by a general

310 decrease towards the hiatus. During MIS 3 phase 2, Sr starts to increase again followed by a

311 decreasing trend, which occurs around 100 mm DFT and is also observed in the Mg record.

312   The $\delta^{18}O_{slc}$ record can be divided into two parts: MIS 3 phase 1 shows, on average, less negative

313   $\delta^{18}O_{slc}$ values (-4.8 ± 0.3 ‰, 1σ SD) than phase 2 (-5.4 ± 0.3 ‰, 1σ SD). In MIS 3 phase 2, the

314   $\delta^{18}O_{slc}$ values show an increasing trend with decreasing DFT.

315   The $\delta^{13}C$ values of both growth phases vary between -5.6 ‰ and -10.4 ‰. MIS 3 phase 1 has

316   a mean $\delta^{13}C$ value of -8.4 ‰ (± 0.8 ‰, 1σ SD) and shows high-frequency variations. MIS 3

317   phase 2 is characterised by a mean value of -8.8 ‰ (± 0.9 ‰, 1σ SD) and shows a rapid

318   decrease from -5.6 ‰ up to approximately -9.0 ‰ between 139 and 130 mm DFT. The

319   youngest section of MIS 3 phase 2 shows a rapid increase of the $\delta^{13}C$ values from -9.8 to -

320   6.2 ‰.

321

322   4.3 Sr-isotopes

323   Bu2 Sr-isotope data show significantly different values for the two growth phases (Fig 5).

324   MIS 3 phase 1 shows $^{87}Sr/^{86}Sr$ ratios between 0.70923 ± 0.00001 and 0.70938 ± 0.00001 (mean

325   value= 0.70931 ± 0.00005, 1σ SD), while ratios for phase 2 are lower (i.e., between 0.70907 ±

326   0.00001 and 0.70919 ± 0.00001, mean value = 0.70915 ± 0.00005, 1σ SD). The Middle to

327   Upper Devonian limestone at Bunker Cave has an average $^{87}Sr/^{86}Sr$ ratio of 0.70836 ± 0.00006

328   (n = 4, 1σ SD, Fig. 5), which is in agreement with the Sr-isotope value expected from the

329   seawater curve (McArthur et al., 2001). Soil horizon A at Bunker Cave has an average Sr

330   isotope ratio of 0.7237 ± 0.0003 (n = 2, 1σ SD, Fig. 5). The $^{87}Sr/^{86}Sr$ ratio of soil horizon C

331   (0.71893 ± 0.00001, n = 1) is lower than the $^{87}Sr/^{86}Sr$ ratio of soil horizon A, but still much

332   more radiogenic than the limestone (Fig. 5).

333

334
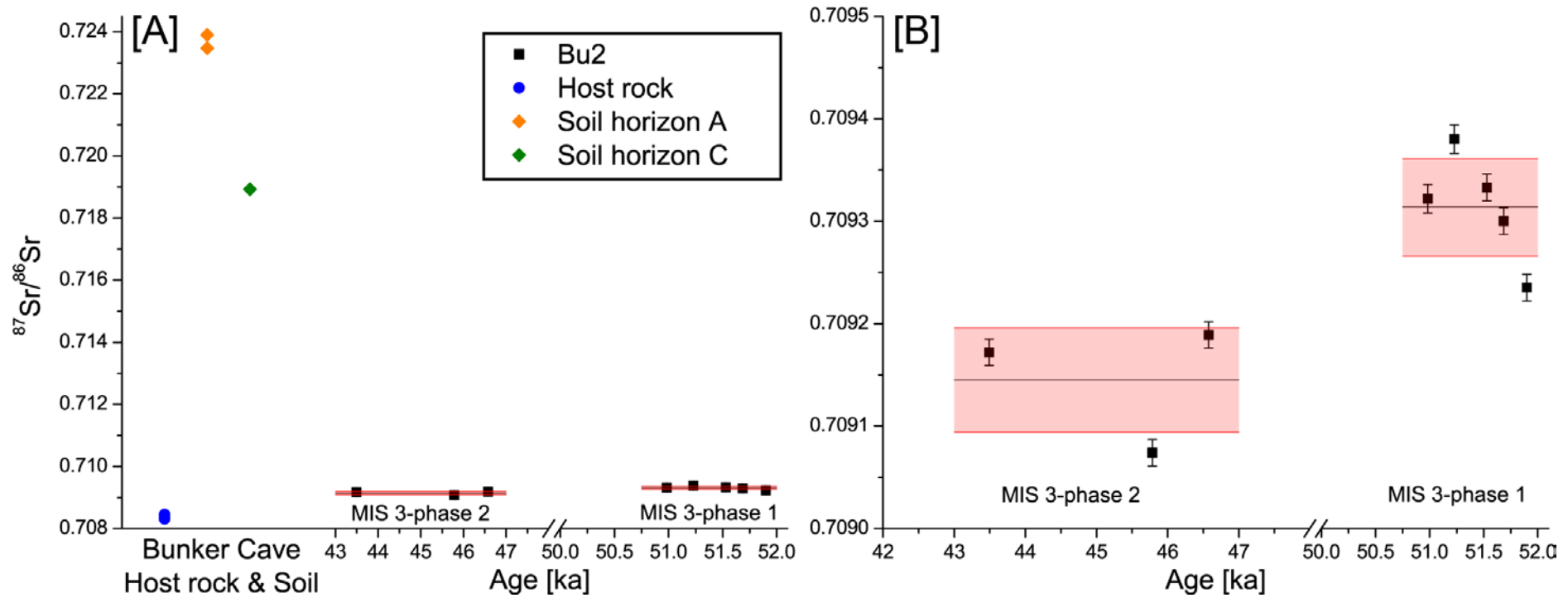
Fig. 5: [A] ^{87}Sr/^{86}Sr ratios of the host rock (blue circle), soil horizon A (orange diamond) and soil horizon C (green diamond) at Bunker Cave compared

to stalagmite Bu2 values (black squares). [B] Close-up of Bu2 ^{87}Sr/^{86}Sr ratios during MIS 3 (black squares). The mean value is shown as a black line

for each phase with the red box indicating the 1σ SD. MIS 3 phase 1 shows generally higher ^{87}Sr/^{86}Sr ratios than MIS 3 phase 2. The soil samples

show much more radiogenic ^{87}Sr/^{86}Sr ratios than the host rock and the speleothem. All measurement uncertainties are 2σ SE.

5. Discussion

5.1. Timing of growth phases

Based on the age-depth model, Bu2 started to grow at 52.0 (+0.8, -0.5) ka with high growth rates between 120 and 390 µm/a. In comparison, the growth rate of Bu2 during the Holocene was only 10 to 30 µm/a. Other Holocene speleothem samples from Bunker Cave also show low growth rates of <30 µm/a (Bu6) and <70 µm/a (Bu4), while a third sample (Bu1) shows growth rates around 100 µm/a (Fohlmeister et al., 2012). In this context, the high growth rate of MIS 3 phase 1 is remarkable, especially for MIS 3 in central Europe. Based on the ^{230}Th/U dating results, MIS 3 phase 1 corresponds to D/O-events 13 and 14 of the NGRIP record. Applying our age-depth model the age range for MIS 3 phase 1 is reduced to between 50.9 (+0.6, -1.3) ka and 52.0 (+0.8, -0.5) ka, rendering a correlation with D/O 14 unlikely. This is interesting given the fact that D/O 14 was the longest interstadial in MIS 3. However, at least the inception of growth of Bu2 may have been related to rather warm and humid conditions during D/O 14, despite the onset of growth was later than D/O 14.

The high growth rate of Bu2 is also exceptional in comparison with other speleothem records from Europe. For instance, the Villars Cave record (Vil-stm9, Genty et al., 2003) shows a growth rate of approximately 100 µm/a during D/O 12 and 10 µm/a during colder periods. Interestingly, Bu2 MIS 3 phase 1 coincides with a flooding event in Villars Cave (Genty et al., 2003; Genty et al., 2005; Genty et al., 2010), expressed by the lack of growth in Vil-stm27, suggesting wet climate conditions during this time interval. A speleothem record from Grotte des Puits de Pierra-la-Treiche (NE France) predates the onset of growth of Bu2 and shows a growth rate between 20 and 80 µm/a for the time period from 55.4 ± 1.0 ka to 53.3 ± 0.7 ka (Pons-Branchu et al., 2010), which is also lower than most parts of MIS 3 phase 1. For Bu2 MIS 3 phase 2 the growth rate is much lower (40 – 50 µm/a until ~46 ka, below 10 µm/a between ~46 and ~42.8 ka), but still higher than in the Holocene. Between 47.3 (+1.0, -0.6) and

364   50.9 (+0.6, -1.3) ka, Bu2 stopped growing. Interestingly, stalagmite Vil-stm14 from Villars

365   Cave showed a significantly diminished growth rate during this period. In contrast, stalagmite

366   Vil-stm27 started to grow at this time around 48.5 ka and shows rapid growth between 47 and

367   44 ka (see supplementary Fig. A3). For this sample, growth inception was probably related to

368   drier conditions subsequent to the flooding event in Villars Cave (Genty et al., 2010).

369   A similar pattern is visible in the speleothem record from Crag Cave (Fankhauser et al., 2016).

370   One of their speleothem samples (CR032) revealed ^{230}Th-ages of 56.8 ± 0.3 ka and 47.9 ± 0.2 ka

371   with a significant brownish layer in between, potentially related to a hiatus during HS 5. A

372   further sample (CR008-B) yielded a ^{230}Th-age of 50.5 ± 0.4 ka, i.e., slightly predating the onset

373   of HS 5 and coinciding within uncertainties with the growth stop of Bu2 at the end of MIS 3

374   phase 1. Combining these records results in a similar growth pattern as observed for Bu2, which

375   shows a hiatus between 50.9 (+0.6, -1.3) ka and 47.3 (+1.0, -0.6) ka and is therefore in good

376   agreement with Crag Cave (Fig. 6). The NALPS composite record (Moseley et al., 2014) shows

377   a similar growth pattern with a slow growth rate between D/O-events 12 and 13 and a short

378   break in speleothem deposition (Fig. 6).

379   The growth stop in Bu2 slightly predates the onset of HS 5 (~49.2 – 47.6 ka, Fig. 6), based on

380   IRD and foraminifera data from the MD99-2331 drill core (Sánchez Goñi et al., 2013). This

381   suggests that the climate at Bunker Cave was too cold and/or dry for speleothem growth even

382   before the onset of HS 5 and that the short-termed D/O 13 was not sufficiently warm and humid

383   to enable speleothem growth at Bunker Cave. This is coherent with the δ^{13}C data (see below).

384   Based on the age uncertainty of MIS 3 phase 1, the offset between the hiatus and the start of

385   HS 5 ranges from 400 to 2000 years.
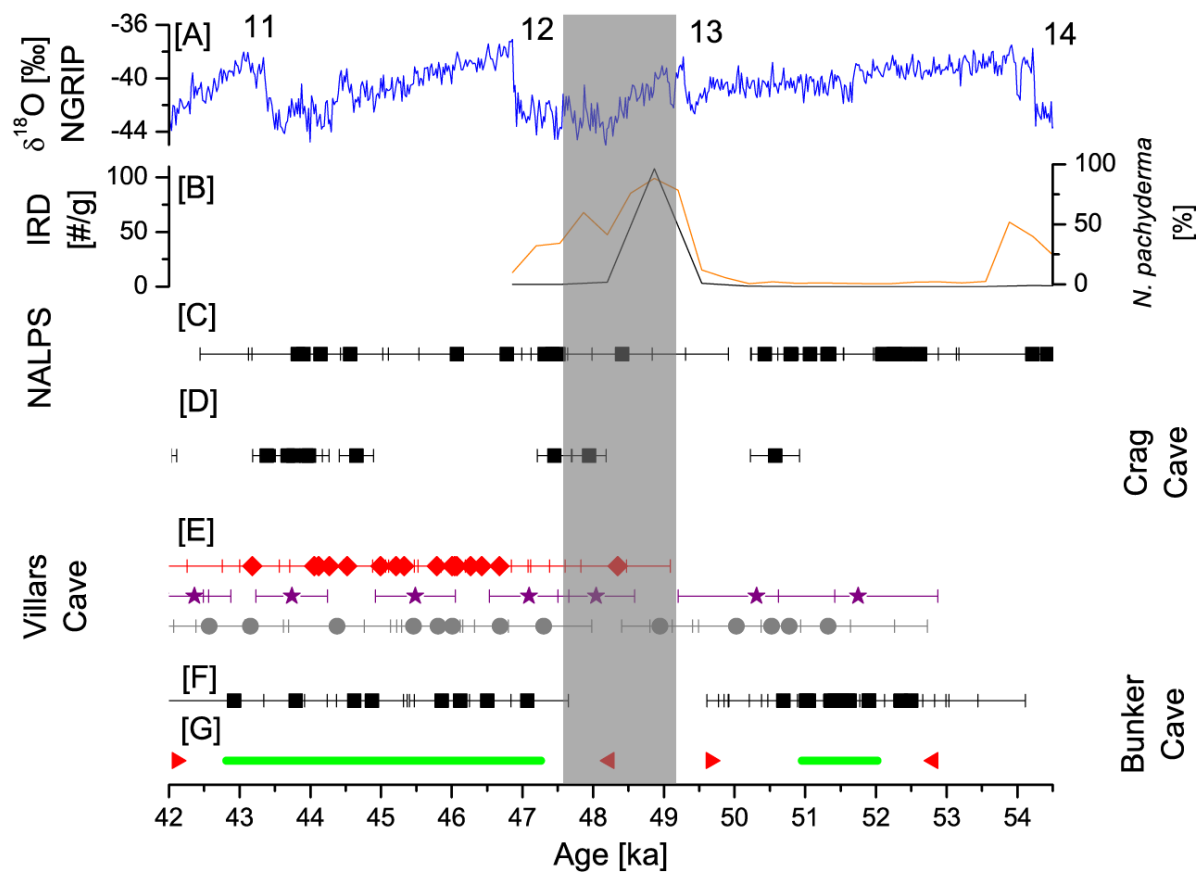
Fig. 6: Comparison of growth phases of different MIS 3 speleothems in Europe with the NGRIP δ^{18}O and the marine MD99-2331 records. [A] NGRIP δ^{18}O record (Svensson et al., 2008). [B] Abundance of the foraminifera *Neogloboquadrina pachyderma* (orange) and the number of IRD per gram of sediment (black) in marine core MD99-2331 (Sánchez Goñi et al., 2013). Heinrich event 5 is marked in the figure (grey box) based on these data. [C] [230]Th/U-ages of the NALPS record (Moseley et al., 2014). [D] [230]Th/U-ages from Crag Cave (Fankhauser et al., 2016). [E] [230]Th/U-ages of stalagmites Vil-stm27 (red diamond, Genty et al., 2010), Vil-stm9 (purple stars, Genty et al., 2010) and Vil-stm14 (grey circles, Wainer et al., 2009) from Villars Cave. [F] [230]Th/U-ages from Bunker Cave stalagmite Bu2 (this study) [G] Growth phases based on the age-depth model (green line) with the respective age uncertainties gives at 95 % confidence levels (red triangles) of Bu2 (this study).

5.2. Bu2 stable isotope data

400   There are several processes potentially affecting the $\delta^{13}C$ values of speleothems. An increase

401   in speleothem $\delta^{13}C$ values may be caused by an increased drip interval and, as a consequence,

402   enhanced disequilibrium fractionation on the stalagmite surface (Deininger et al., 2012;

403   Mühlinghaus et al., 2009; Riechelmann et al., 2013; Scholz et al., 2009). Furthermore, an

404   increase of the $\delta^{13}C$ values can be caused due to a larger contribution of host rock-derived

405   carbon or a decrease in the soil CO_2 production rate by reduced root respiration and soil

406   microbial activity (Cerling, 1984; Fohlmeister et al., 2011). Monitoring of Bunker Cave

407   (Riechelmann et al., 2011) showed only small variations in the present-day annual $\delta^{13}C$ values

408   of the dissolved inorganic carbon (DIC) of the drip water, collected at different drip sites of the

409   cave. Modern calcite precipitation from a drip site close to the location where Bu2 was collected

410   (watch glass VII, Riechelmann, 2010) revealed an average $\delta^{13}C$-value of -8.6 ± 0.6 ‰, which

411   is in the range of the more positive $\delta^{13}C$ values of the MIS 3 growth phase of Bu2 (Fig. 7). As

412   described by Fohlmeister et al. (2012), vegetation density above Bunker Cave is assumed to be

413   the major factor influencing the $\delta^{13}C$ values of speleothems. More positive $\delta^{13}C$ values of soil

414   gas CO_2 will therefore also yield increased $\delta^{13}C$ values in the stalagmite, coherent with periods

415   of lower drip rates. In contrast, more negative $\delta^{13}C$ values in the speleothem are associated with

416   periods of denser vegetation as well as a thickening of the soil above the cave, increased

417   biological soil activity and higher drip rates. The most negative $\delta^{13}C$ values during MIS 3 are

418   in the range of the $\delta^{13}C$ values of the Holocene stalagmites and modern-day calcite samples

419   (Fig. 7). This indicates, at least for some time intervals of MIS 3, an enhanced biological

420   activity above the cave, almost as high as for present-day conditions.

421   Prior to the hiatus around 50.9 ka, the $\delta^{13}C$ values increase rapidly from around -9 ‰ to -5.5 ‰

422   (Fig. 8). This suggests a decrease in vegetation density and soil bioproductivity, resulting in

423   more positive $\delta^{13}C$ values of soil gas CO_2 and ultimately in Bu2, similar to the $\delta^{13}C$ values of

424   Villars Cave speleothem Vil-stm9 around the MIS 4 cold period (Genty et al., 2010). This

425   climate deterioration recorded in Bu2 precedes the onset of HS 5 (~49.2 – 47.6 ka, Fig. 8) and

426   implies that the climate at Bunker Cave was too cold and/or dry even before the onset of HS 5,

427   potentially due to gradual cooling towards HS 5 and insufficient warming during D/O 13,

428   related to its short duration.

429   Bu2 started to grow again at ~47.3 ka with similar $\delta^{13}C$ values as prior to the hiatus (-5.5 ‰,

430   Fig. 8). The following decrease in $\delta^{13}C$ values to ~-9 ‰ is associated with D/O 12 and occurred

431   relatively slowly, in particular in comparison to other climate records, such as the $\delta^{18}O$ values

432   of NGRIP and NALPS (Fig. 8). This may be related to biological and/or buffering processes in

433   the soil, which are likely to occur on longer time scales than the processes controlling the $\delta^{18}O$

434   values of precipitation. Although in a different climate setting, a similar discrepancy between

435   the evolution of $\delta^{13}C$ and $\delta^{18}O$ values in response to rapid climate change within a single

436   stalagmite has been shown for Sofular Cave (Fleitmann et al., 2009). Another explanation for

437   the discrepancy of the duration of the transition into D/O 12 are the dating uncertainties of the

438   individual records, which is in the range of a few hundred years, in particular for the stalagmite

439   records (Fig. 6). In general, the $\delta^{13}C$ values of Bu2 show a D/O-like pattern as the $\delta^{18}O$ values

440   of the NGRIP (Svensson et al., 2008) and NALPS records (Moseley et al., 2014), making the

441   correlation with D/O 12 plausible. The later part of MIS 3 phase 2 is characterised by rather

442   stable $\delta^{13}C$ values around -9 to -10 ‰ until ~44.5 ka (Fig. 8). Subsequently, the $\delta^{13}C$ values

443   increase until 44.1 ka, followed by a decrease by about 1 ‰, which, however, is insignificant

444   compared to the overall change in $\delta^{13}C$ during MIS 3 phase 2. Thus, although the timing of this

445   decrease is synchronous within error with D/O 11 in the NALPS and NGRIP $\delta^{18}O$ records

446   (Fig. 8), we cannot precisely identify D/O 11 in the Bu2 $\delta^{13}C$ record. This finding is coherent

447   with the Villars Cave record, where D/O 11 is also not obvious; probably due to its short

448   duration (Genty et al., 2010). However, the significant increase in $\delta^{13}C$ values after ~43.3 ka

449   indicates a climate deterioration, associated with the cooling phase after D/O 11. While the

450   NAPLS record shows a growth stop during D/O 11, the Bu2 record shows a growth stop after

451   D/O 11, about 1000 years later. In contrast to the NALPS stalagmites, growth of the Bu2

452   stalagmite did not recommence until the onset of the Holocene, probably related to a further

453   European cooling trend after ~45 ka, as described in the Villars Cave record (Genty et al.,

454   2010).

455   The $\delta^{18}O_{slc}$ values of Bu2 do neither show a similar pattern as the $\delta^{13}C$ values (Fig. 7) nor strong

456   variability during D/O-events, as would be expected from other records (NGRIP, NALPS,

457   Fig. 8). MIS 3 phase 1 shows higher $\delta^{18}O_{slc}$ values than phase 2. In addition, the second growth

458   phase shows progressively increasing $\delta^{18}O_{slc}$ values. In general, the interpretation of the $\delta^{18}O$

459   values of Bu2 in terms of past climate variability is challenging, as has also been shown for

460   other speleothems from central Europe (e.g., Mischel et al., 2016; Scholz et al., 2012).

461   Therefore, the discussion of the $\delta^{18}O$ values is only provided in the supplement.
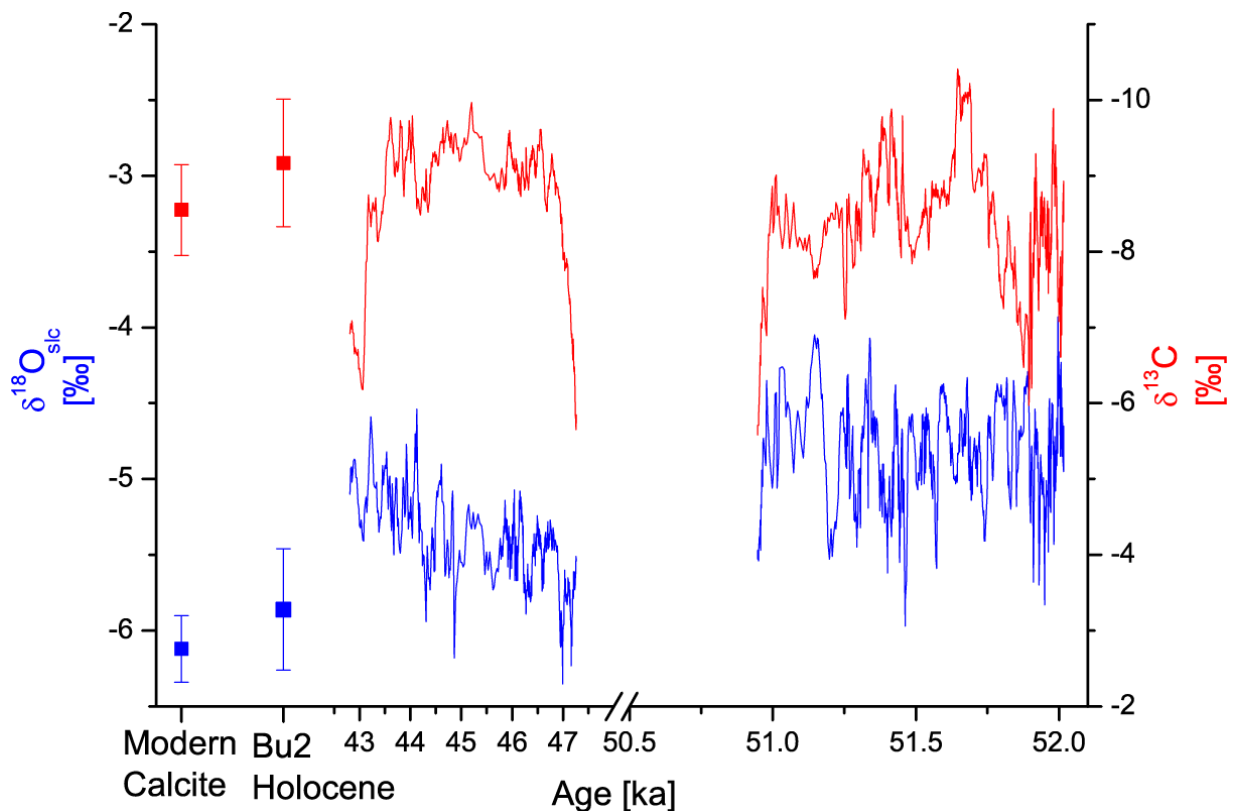
463   **Fig. 7:** Speleothem Bu2 $\delta^{13}C$ (red) and $\delta^{18}O_{slc}$ (blue) record plotted against age. Also shown

464   are the $\delta^{13}C$ and $\delta^{18}O$ values from modern calcite precipitated on watch glasses (Riechelmann,

465   2010) placed under a drip site (TS 7) close to the Bu2 drip site and the Holocene section of Bu2

466   (Fohlmeister et al., 2012). Note that the $\delta^{13}C$ axis is inverted.

467

5.3. Palaeoclimate implications

The Bunker Cave system has been intensively studied by both cave monitoring (Immenhauser et al., 2010; Riechelmann et al., 2011; Riechelmann et al., 2013; Riechelmann et al., 2012b; Riechelmann et al., 2014; Riechelmann et al., 2017) and speleothem-based palaeoclimate reconstructions (Fohlmeister et al., 2012; Riechelmann et al., 2012a). Based on the findings of von Kamp and Ribbert (2005), Fohlmeister et al. (2012) argued that loess with a higher Mg/Ca ratio than the Devonian limestone host rock was deposited above Bunker Cave during the last glacial maximum (LGM). They assumed that progressive leaching of this wind-blown dust resulted in elevated Mg/Ca ratios in the drip water and the speleothems at the beginning of the Holocene. MIS 3 phase 1 (52.0 – 50.9 ka) shows significantly lower Mg values compared to MIS 3 phase 2 (Fig. 4). Thus, the increase in the Mg/Ca ratio from MIS 3 phase 1 to phase 2 may be related to loess deposition during HS 5. This is consistent with the data of von Kamp and Ribbert (2005), who suggested loess deposition in the area around Bunker Cave during MIS 3. However, both speleothem growth phases show lower Mg/Ca ratios than during the Holocene. Since the Mg-content of loess can be highly variable (Gallet et al., 1998; Taylor et al., 1983), this may be related to different Mg/Ca ratios of the LGM and the MIS 3 loess. The Mg/Ca ratio of the loess above Bunker Cave has not been determined.

Another factor potentially affecting the Mg-concentration of speleothems in Bunker Cave is prior calcite precipitation (PCP, Fairchild et al., 2000; Riechelmann et al., 2011), which accounts for calcite precipitation from the parent solution prior to dripping on top of the stalagmite. Reduced infiltration in the catchment above the cave will result in an increase of the residence time of the water in the host rock and in reduced drip rates. This results in increased PCP, which, in turn, results in increasing Mg/Ca ratios (Tooth and Fairchild, 2003). A third potential explanation affecting the Mg/Ca ratios of speleothems at Bunker Cave are the different

492   dissolution characteristics of calcite and dolomite (Fairchild and Treble, 2009). With increasing

493   residence times, the relative contribution from dissolution of dolomite will increase and

494   therefore result in elevated Mg/Ca ratios of the drip water and the speleothem. In summary,

495   those mechanisms suggest increasing Mg/Ca ratios during dry conditions. In general, the Mg-

496   concentration of Bunker Cave speleothems can, thus, be used as a proxy for precipitation

497   amount (Fohlmeister et al., 2012; Wassenburg et al., 2016). Thus, the lower Mg-concentration

498   of MIS 3 phase 1 indicates more humid conditions than during MIS 3 phase 2. This is also

499   supported by the much higher growth rate during MIS 3 phase 1, which suggests higher rainfall

500   amounts.

501   The Sr isotope ratio of all Bu2 samples is significantly higher than expected from the overlying

502   hostrock, indicating an external radiogenic source. In most cases, this additional material is

503   incorporated in the soil above the cave area, e.g. by deposition of atmospheric dust (e.g., Banner

504   et al., 1996; Frumkin and Stein, 2004; Zhou et al., 2009). We argue that the changes in the Sr-

505   isotope ratio of Bu2 are mainly attributed to changes in rainfall intensity and/or changes in soil

506    $p\mathrm{CO_2}$ resulting in varying Sr contribution from the soil and host rock. Smart and Friedrich

507   (1987) developed a model where different amounts of rainfall caused changes in the routes of

508   vadose ground-water flow. This model was adapted by Banner et al. (1996) and applied to the

509   Sr isotope composition of the Barbados karst system. According to these studies, changes in

510   the amount of rainfall above the cave affect the pathway of the water in the karst aquifer. During

511   periods of diminished rainfall, the drip water preferentially percolates along seepage routes.

512   During periods of elevated rainfall, the capacity of these seepages routes is exceeded, and the

513   drip water is transported into the cave by conduit flow along paths with a higher permeability,

514   resulting in an overflow (Riechelmann et al., 2011). This results in a decreased residence time

515   and a reduced interaction of the percolating water with the host rock. Hence, we expect that the

516   drip water composition and, ultimately, the Sr isotope signature of the speleothem sample, will

517   evolve towards the soil signature ($^{87}\mathrm{Sr}/^{86}\mathrm{Sr} > 0.718$) during times of elevated rainfall. In

518   contrast, periods with lower rainfall amounts should be characterised by a speleothem $^{87}Sr/^{86}Sr$

519   ratio shifted towards the host rock signature ($^{87}Sr/^{86}Sr = 0.70836 \pm 0.00006$). These patterns are

520   clearly visible in the Bu2 $^{87}Sr/^{86}Sr$ record. MIS 3 phase 1, which exhibits a faster growth rate,

521   shows an average $^{87}Sr/^{86}Sr$ ratio of 0.70931 ± 0.00005 (1σ SD), significantly more radiogenic

522   than MIS 3 phase 2. The latter, growing at a slower growth rate, shows an average $^{87}Sr/^{86}Sr$

523   ratio of 0.70915 ± 0.00005 (1σ SD). Both the large growth rate and the Sr isotope signatures

524   therefore indicate enhanced rainfall and infiltration during MIS 3 phase 1, consistent with the

525   Mg record. A further explanation would be changes of drip water $^{87}Sr/^{86}Sr$ due to changes in

526   the weathering of soil components as a result of differences in soil pCO_2 (Banner et al., 1996).

527   Sr-isotopes are widely used in the soil environment to trace weathering processes (Capo et al.,

528   1998; Stewart et al., 1998). The most likely external soil component is loess, potentially

529   deposited during MIS 4 and HS 5 in the Bunker Cave area (von Kamp and Ribbert, 2005). This

530   loess usually has a high Si-content (Gallet et al., 1998) and a highly radiogenic $^{87}Sr/^{86}Sr$ ratio

531   (Taylor et al., 1983). During warm periods with increased biological activity, as suggested for

532   MIS 3 phase 1, weathering of silicate material is enhanced resulting in increased input of

533   radiogenic Sr into the drip water and the speleothems. It is likely that the Sr-isotope composition

534   of the drip water was affected by both mechanisms
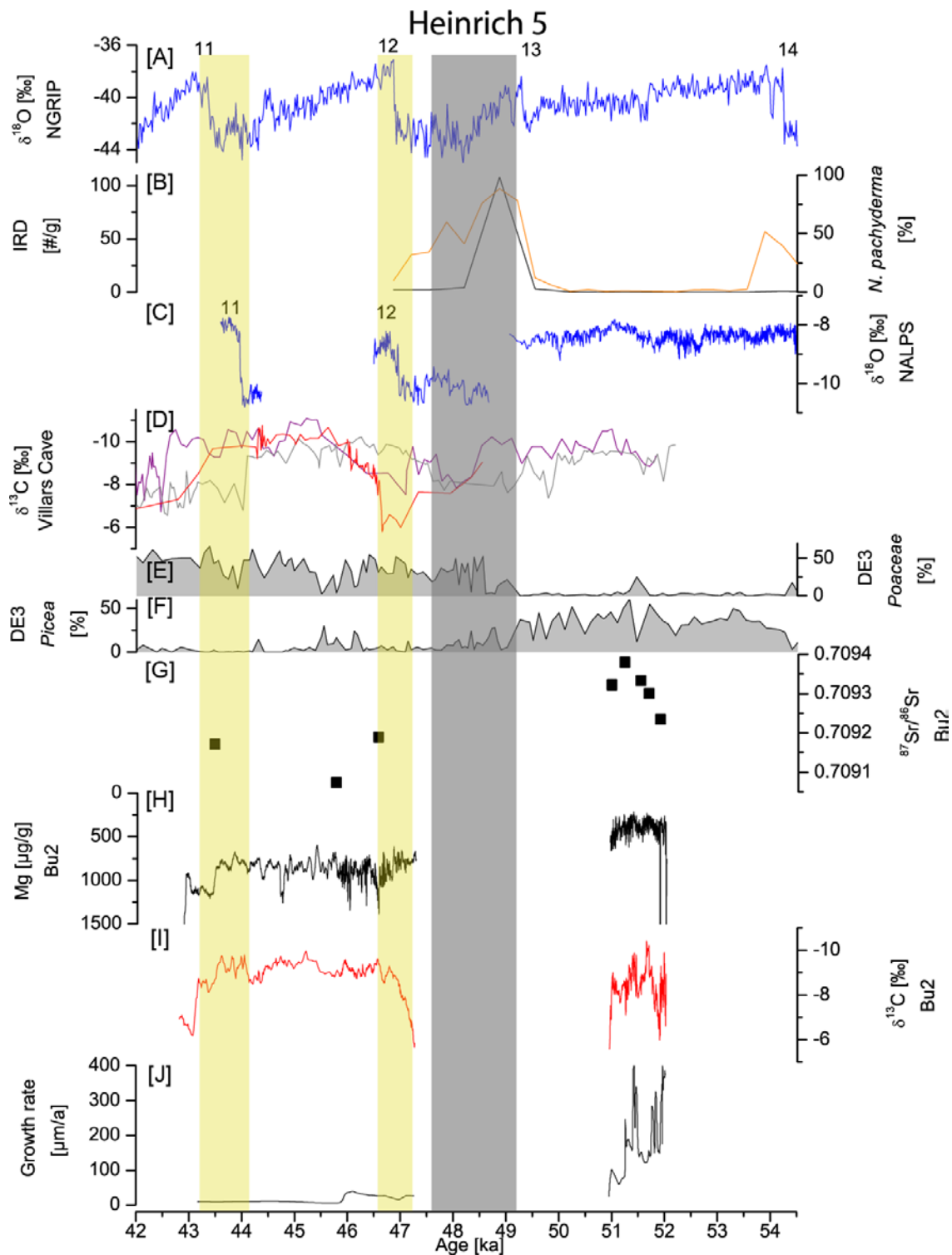
Fig. 8: Comparison of the Bu2 multi-proxy record with other MIS 3 climate records. Yellow boxes show the timing of D/O-events 12 and 11. [A] NGRIP δ18O record (Svensson et al., 2008). [B] Abundance of the foraminifera *Neogloboquadrina pachyderma* (orange) and the number of IRD per gram of sediment (black) in marine core MD99-2331 (Sánchez Goñi et al., 2013). Heinrich 5 event is marked in the figure (grey box) based on these data. [C] NALPS

541   oxygen isotope record from alpine speleothem samples (Moseley et al., 2014). [D] Villars Cave

542   stable carbon isotope records, Vil-stm9 (purple), Vil-stm14 (grey), Vil-stm27 (red, Genty et al.,

543   2003; Genty et al., 2010; Wainer et al., 2009) [E] Percentage of *Poaceae*-pollen in drill core

544   DE3 from the Eifel, Germany (Sirocko et al., 2016). [F] Percentage of *Picea*-pollen in drill core

545   DE3 from the Eifel, Germany (Sirocko et al., 2016). [G] Sr-isotope data of Bu2. [H] Mg

546   concentration of Bu2. [I] δ^{13}C values of Bu2. Note inverted axis for Mg concentrations and δ^{13}C

547   values. [J] Growth rate of Bu2.

548

549   Although the minimum δ^{13}C values of the two MIS 3 growth phases of Bu2 are similar, the

550   other proxy data (Sr-isotopes, Mg concentration, growth rate, Fig. 8) suggest that MIS 3 phase 1

551   was characterised by a generally more humid climate compared to MIS 3 phase 2, in agreement

552   with pollen records from the Eifel (Sirocko et al., 2016). The latter show more abundant *Picea*

553   and *Carpinus* pollen during MIS 3 phase 1 (Fig. 8). Both plant species are indicators of rather

554   humid and relatively warm conditions, indicating summer temperatures only slightly lower than

555   modern-day temperatures, thus suggesting a mild climate during early MIS 3. High abundance

556   of *Poaceae* pollen indicate dry conditions and open landscapes with less dense vegetation

557   during MIS 3 phase 2, which was characterised by (at least seasonal) aridity indicated by the

558   very low abundance of *Pinus* (Fig. 8). This implies a more open boreal forest with generally

559   drier conditions. Interestingly, this change in vegetation is not reflected in the δ^{13}C record of

560   our speleothem, potentially related to colder conditions in the Eifel than in nearby areas

561   (Sirocko et al., 2016). Although precipitation decreased, it was obviously still sufficiently

562   humid to enable vegetation and soil development above Bunker Cave, at least until the δ^{13}C

563   values increased again around 43.5 ka. The high δ^{13}C values around 43 ka, shortly before the

564   growth stop, coincide with Greenland Stadial 11 (Rasmussen et al., 2014). Consequently, a

565   severe climate deterioration seems to be the most plausible cause for the increase of the δ^{13}C

566 values and Mg concentration, as well as the following growth stop, possibly amplified by

567 disequilibrium isotope fractionation on the stalagmite surface induced by a very slow drip rate

568 (Deininger et al., 2012; Mühlinghaus et al., 2009). This is supported by the very low growth

569 rate of <10 µm/a towards the end of MIS 3 phase 2.

570 Overall, Bu2 recorded two generally humid and warm phases during early MIS 3. Based on the

571 proxy data, the two growth phases were characterised by different climate conditions. While

572 MIS 3 phase 1 was humid and warm, we observe a significant decrease in water availability

573 subsequent to the hiatus associated with HS 5. However, climatic and environmental conditions

574 were still favourable for speleothem growth at Bunker Cave. Thus, we assume that MIS 3

575 phase 2 was still a comparably humid and warm period, although it was probably drier and

576 colder than during the first MIS 3 growth phase.

577

578 **6. Conclusions**

579 Speleothem Bu2 from Bunker Cave offers the possibility to investigate past climate variability

580 during two early phases of MIS 3 north of the Alps in central Europe. This MIS 3 speleothem

581 record shows that the climatic conditions during this phase were, at least during some parts,

582 favourable of speleothem growth. Therefore, speleothem Bu2 potentially recorded the two

583 warmest and most humid phases of MIS 3 in central Europe.

584 The timing of the hiatus between the two growth phases is coherent with HS 5 (Sánchez Goñi

585 et al., 2013). The high growth rate, the elevated Sr-isotopes and the low Mg content suggest

586 increased water availability and enhanced precipitation during the initial MIS 3 growth phase

587 of Bu2. This is further supported by the occurrence of thermophilous trees in a nearby Eifel

588 pollen record (Sirocko et al., 2016). During the second MIS 3 growth phase, precipitation was

589 substantially lower, as suggested by the slower growth rate, the lower Sr-isotope ratios and the

590   higher Mg content. This is consistent with the evidence of boreal forests in the Eifel (Sirocko

591   et al., 2016). The $\delta^{13}C$ values clearly reflect D/O event 12, while the $\delta^{18}O$ record does not show

592   a D/O-type pattern.

593

602   **References**

603

604   Bajo, P., Hellstrom, J., Frisia, S., Drysdale, R., Black, J., Woodhead, J., Borsato, A., Zanchetta,
605   G., Wallace, M.W., Regattieri, E., Haese, R., 2016. "Cryptic" diagenesis and its implications
606   for speleothem geochronologies. Quaternary Science Reviews 148, 17-28.
607   Baker, A., Smart, P.L., Ford, D.C., 1993. Northwest European palaeoclimate as indicated by
608   growth   frequency   variations   of   secondary   calcite   deposits.   Palaeogeography,
609   Palaeoclimatology, Palaeoecology 100, 291-301.
610   Banner, J.L., Musgrove, M.L., Asmerom, Y., Edwards, R.L., Hoff, J.A., 1996. High-resolution
611   temporal record of Holocene ground-water chemistry: Tracing links between climate and
612   hydrology. Geology 24, 1049-1053.
613   Bates, S.L., Siddall, M., Waelbroeck, C., 2014a. Sea level records and deep ocean temperatures
614   from ODP composite site 162-980/981, In supplement to: Bates, SL et al. (2014): Hydrographic
615   variations in deep ocean temperature over the mid-Pleistocene transition. Quaternary Science
616   Reviews, 88, 147-158, https://doi.org/10.1016/j.quascirev.2014.01.020. PANGAEA.
617   Bates, S.L., Siddall, M., Waelbroeck, C., 2014b. Hydrographic variations in deep ocean
618   temperature over the mid-Pleistocene transition. Quaternary Science Reviews 88, 147-158.
619   Böhm, E., Lippold, J., Gutjahr, M., Frank, M., Blaser, P., Antz, B., Fohlmeister, J., Frank, N.,
620   Andersen, M.B., Deininger, M., 2015. Strong and deep Atlantic meridional overturning
621   circulation during the last glacial cycle. Nature 517, 73.
622   Bond, G., Broecker, W., Johnsen, S., McManus, J., Labeyrie, L., Jouzel, J., Bonani, G., 1993.
623   Correlations between climate records from North Atlantic sediments and Greenland ice. Nature
624   365, 143-147.
625   Cacho, I., Grimalt, J.O., Pelejero, C., Canals, M., Sierro, F.J., Flores, J.A., Shackleton, N., 1999.
626   Dansgaard-Oeschger and Heinrich event imprints in Alboran Sea paleotemperatures.
627   Paleoceanography 14, 698-705.
628   Capo, R.C., Stewart, B.W., Chadwick, O.A., 1998. Strontium isotopes as tracers of ecosystem
629   processes: theory and methods. Geoderma 82, 197-225.
630   Cerling, T.E., 1984. The stable isotopic composition of modern soil carbonate and its
631   relationship to climate. Earth and Planetary Science Letters 71, 229-240.
632   Constantin, S., Bojar, A.-V., Lauritzen, S.-E., Lundberg, J., 2007. Holocene and Late
633   Pleistocene climate in the sub-Mediterranean continental environment: a speleothem record
634   from Poleva Cave (Southern Carpathians, Romania). Palaeogeography, Palaeoclimatology,
635   Palaeoecology 243, 322-338.
636   Dansgaard, W., Johnsen, S.J., Clausen, H.B., Dahl-Jensen, D., Gundestrup, N.S., Hammer,
637   C.U., Hvidberg, C.S., Steffensen, J.P., Sveinbjörnsdottir, A.E., Jouzel, J., 1993. Evidence for
638   general instability of past climate from a 250-kyr ice-core record. Nature 364, 218-220.
639   Deininger, M., Fohlmeister, J., Scholz, D., Mangini, A., 2012. Isotope disequilibrium effects:
640   The influence of evaporation and ventilation effects on the carbon and oxygen isotope
641   composition of speleothems – A model approach. Geochimica et Cosmochimica Acta 96, 57-
642   79.
643   Duplessy, J.C., Roche, D.M., Kageyama, M., 2007. The Deep Ocean During the Last
644   Interglacial Period. Science 316, 89.
645   Fairchild, I.J., Borsato, A., Tooth, A.F., Frisia, S., Hawkesworth, C.J., Huang, Y., McDermott,
646   F., Spiro, B., 2000. Controls on trace element (Sr–Mg) compositions of carbonate cave waters:
647   implications for speleothem climatic records. Chemical Geology 166, 255-269.

Fairchild, I.J., Smith, C.L., Baker, A., Fuller, L., Spotl, C., Mattey, D., McDermott, F., Eimp, 2006. Modification and preservation of environmental signals in speleothems. Earth-Science Reviews 75, 105-153.

Fairchild, I.J., Treble, P.C., 2009. Trace elements in speleothems as recorders of environmental change. Quaternary Science Reviews 28, 449-468.

Fankhauser, A., McDermott, F., Fleitmann, D., 2016. Episodic speleothem deposition tracks the terrestrial impact of millennial-scale last glacial climate variability in SW Ireland. Quaternary science reviews 152, 104-117.

Fleitmann, D., Cheng, H., Badertscher, S., Edwards, R.L., Mudelsee, M., Göktürk, O.M., Fankhauser, A., Pickering, R., Raible, C.C., Matter, A., Kramers, J., Tüysüz, O., 2009. Timing and climatic impact of Greenland interstadials recorded in stalagmites from northern Turkey. Geophysical Research Letters 36.

Fohlmeister, J., Scholz, D., Kromer, B., Mangini, A., 2011. Modelling carbon isotopes of carbonates in cave drip water. Geochimica et Cosmochimica Acta 75, 5219-5228.

Fohlmeister, J., Schröder-Ritzrau, A., Scholz, D., Spötl, C., Riechelmann, D.F.C., Mudelsee, M., Wackerbarth, A., Gerdes, A., Riechelmann, S., Immenhauser, A., Richter, D.K., Mangini, A., 2012. Bunker Cave stalagmites: an archive for central European Holocene climate variability. Clim. Past 8, 1751-1764.

Frumkin, A., Stein, M., 2004. The Sahara-East Mediterranean dust and climate connection revealed by strontium and uranium isotopes in a Jerusalem speleothem. Earth and Planetary Science Letters 217, 451-464.

Gallet, S., Jahn, B.M., Lanoe, B.V., Dia, A., Rossello, E., 1998. Loess geochemistry and its implications for particle origin and composition of the upper continental crust. Earth and Planetary Science Letters 156, 157-172.

Genty, D., Blamart, D., Ouahdi, R., Gilmour, M., Baker, A., Jouzel, J., Van-Exter, S., 2003. Precise dating of Dansgaard-Oeschger climate oscillations in western Europe from stalagmite data. Nature 421, 833-837.

Genty, D., Combourieu Nebout, N., Hatté, C., Blamart, D., Ghaleb, B., Isabello, L., 2005. Rapid climatic changes of the last 90 kyr recorded on the European continent. Comptes Rendus Geoscience 337, 970-982.

Genty, D., Combourieu-Nebout, N., Peyron, O., Blamart, D., Wainer, K., Mansuri, F., Ghaleb, B., Isabello, L., Dormoy, I., von Grafenstein, U., Bonelli, S., Landais, A., Brauer, A., 2010. Isotopic characterization of rapid climatic events during OIS3 and OIS4 in Villars Cave stalagmites (SW-France) and correlation with Atlantic and Mediterranean pollen records. Quaternary Science Reviews 29, 2799-2820.

Gerdes, A., Zeh, A., 2006. Combined U–Pb and Hf isotope LA-(MC-)ICP-MS analyses of detrital zircons: Comparison with SHRIMP and new constraints for the provenance and age of an Armorican metasediment in Central Germany. Earth and Planetary Science Letters 249, 47-61.

Gibert, L., Scott, G.R., Scholz, D., Budsky, A., Ferràndez, C., Ribot, F., Martin, R.A., Lería, M., 2016. Chronology for the Cueva Victoria fossil site (SE Spain): Evidence for Early Pleistocene Afro-Iberian dispersals. Journal of Human Evolution 90, 183-197.

Gordon, D., Smart, P.L., Ford, D.C., Andrews, J.N., Atkinson, T.C., Rowe, P.J., Christopher, N.S.J., 1989. Dating of late Pleistocene interglacial and interstadial periods in the United Kingdom from speleothem growth frequency. Quaternary Research 31, 14-26.

Grebe, W., 1993. Die Bunkerhöhle in Iserlohn-Letmathe (Sauerland). Mitteilung des Verbands der deutschen Höhlen-und Karstforscher, München 39, 22-23.

Heinrich, H., 1988. Origin and Consequences of Cyclic Ice Rafting in the Northeast Atlantic Ocean During the Past 130,000 Years. Quaternary Research 29, 142-152.

Hennig, G.J., Grün, R., Brunnacker, K., 1983. Speleothems, travertines, and paleoclimates. Quaternary Research 20, 1-29.

Hodge, E.J., Richards, D.A., Smart, P.L., Andreo, B., Hoffmann, D.L., Mattey, D.P., González-Ramón, A., 2008. Effective precipitation in southern Spain (~ 266 to 46 ka) based on a speleothem stable carbon isotope record. Quaternary Research 69, 447-457.

Hoffmann, D.L., Prytulak, J., Richards, D.A., Elliott, T., Coath, C.D., Smart, P.L., Scholz, D., 2007. Procedures for accurate U and Th isotope measurements by high precision MC-ICPMS. International Journal of Mass Spectrometry 264, 97-109.

Hoffmann, D.L., 2008. 230Th isotope measurements of femtogram quantities for U-series dating using multi ion counting (MIC) MC-ICPMS. International Journal of Mass Spectrometry 275, 75-79.

Holzkämper, S., Spötl, C., Mangini, A., 2005. High-precision constraints on timing of Alpine warm periods during the middle to late Pleistocene using speleothem growth periods. Earth and Planetary Science Letters 236, 751-764.

Huber, C., Leuenberger, M., Spahni, R., Flückiger, J., Schwander, J., Stocker, T.F., Johnsen, S., Landais, A., Jouzel, J., 2006. Isotope calibrated Greenland temperature record over Marine Isotope Stage 3 and its relation to CH4. Earth and Planetary Science Letters 243, 504-519.

Immenhauser, A., Buhl, D., Richter, D., Niedermayr, A., Riechelmann, D., Dietzel, M., Schulte, U., 2010. Magnesium-isotope fractionation during low-Mg calcite precipitation in a limestone cave–Field study and experiments. Geochimica et Cosmochimica Acta 74, 4346-4364.

Jochum, K.P., Nohl, L., Herwig, K., Lammel, E., Stoll, B., Hofmann, A.W., 2005. GeoReM: A new geochemical database for reference materials and isotopic standards. Geostandards and Geoanalytical Research 29, 333-338.

Jochum, K.P., Weis, U., Stoll, B., Kuzmin, D., Yang, Q., Raczek, I., Jacob, D.E., Stracke, A., Birbaum, K., Frick, D.A., 2011. Determination of reference values for NIST SRM 610–617 glasses following ISO guidelines. Geostandards and Geoanalytical Research 35, 397-429.

Jochum, K.P., Scholz, D., Stoll, B., Weis, U., Wilson, S.A., Yang, Q.C., Schwalb, A., Borner, N., Jacob, D.E., Andreae, M.O., 2012. Accurate trace element analysis of speleothems and biogenic calcium carbonates by LA-ICP-MS. Chemical Geology 318, 31-44.

Johnsen, S.J., Clausen, H.B., Dansgaard, W., Fuhrer, K., Gundestrup, N., Hammer, C.U., Iversen, P., Jouzel, J., Stauffer, B., 1992. Irregular glacial interstadials recorded in a new Greenland ice core. Nature 359, 311-313.

Kindler, P., Guillevic, M., Baumgartner, M., Schwander, J., Landais, A., Leuenberger, M., 2014. Temperature reconstruction from 10 to 120 kyr b2k from the NGRIP ice core. Climate of the Past 10, 887-902.

Lachniet, M.S., 2009. Climatic and environmental controls on speleothem oxygen-isotope values. Quaternary Science Reviews 28, 412-432.

Lisiecki, L.E., Raymo, M.E., 2005. A Pliocene-Pleistocene stack of 57 globally distributed benthic δ18O records. Paleoceanography 20, n/a-n/a.

Luetscher, M., Boch, R., Sodemann, H., Spotl, C., Cheng, H., Edwards, R.L., Frisia, S., Hof, F., Muller, W., 2015. North Atlantic storm track changes during the Last Glacial Maximum recorded by Alpine speleothems. Nat Commun 6, 6344.

Lugli, F., Cipriani, A., Peretto, C., Mazzucchelli, M., Brunelli, D., 2017. In situ high spatial resolution $^{87}Sr/^{86}Sr$ ratio determination of two Middle Pleistocene (c.a. 580 ka) Stephanorhinus hundsheimensis teeth by LA–MC–ICP–MS. International Journal of Mass Spectrometry 412, 38-48.

Mangini, A., Verdes, P., Spötl, C., Scholz, D., Vollweiler, N., Kromer, B., 2007. Persistent influence of the North Atlantic hydrography on central European winter temperature during the last 9000 years. Geophysical Research Letters 34.

Mattey, D.P., Atkinson, T.C., Barker, J.A., Fisher, R., Latin, J.P., Durrell, R., Ainsworth, M., 2016. Carbon dioxide, ground air and carbon cycling in Gibraltar karst. Geochimica et Cosmochimica Acta 184, 88-113.

749   McArthur, J.M., Howarth, R.J., Bailey, T.R., 2001. Strontium Isotope Stratigraphy: LOWESS
750   Version 3: Best Fit to the Marine Sr-Isotope Curve for 0–509 Ma and Accompanying Look-up
751   Table for Deriving Numerical Age. Journal of Geology 109, 155-170.
752   McDermott, F., Frisia, S., Huang, Y., Longinelli, A., Spiro, B., Heaton, T.H.E., Hawkesworth,
753   C.J., Borsato, A., Keppens, E., Fairchild, I.J., 1999. Holocene climate variability in Europe:
754   evidence from δ18O, textural and extension-rate variations in three speleothems. Quaternary
755   Science Reviews 18, 1021-1038.
756   McDermott, F., 2004. Palaeo-climate reconstruction from stable isotope variations in
757   speleothems: a review. Quaternary Science Reviews 23, 901-918.
758   Mischel, S.A., Scholz, D., Spötl, C., Jochum, K.P., Schröder-Ritzrau, A., Fiedler, S., 2016.
759   Holocene climate variability in Central Germany and a potential link to the polar North Atlantic:
760   A replicated record from three coeval speleothems. The Holocene 27, 509-525.
761   Mischel, S.A., Mertz‐Kraus, R., Jochum Klaus, P., Scholz, D., 2017. TERMITE: An R script
762   for fast reduction of laser ablation inductively coupled plasma mass spectrometry data and its
763   application to trace element measurements. Rapid Communications in Mass Spectrometry 31,
764   1079-1087.
765   Moseley, G.E., Spötl, C., Svensson, A., Cheng, H., Brandstätter, S., Edwards, R.L., 2014.
766   Multi-speleothem record reveals tightly coupled climate between central Europe and Greenland
767   during Marine Isotope Stage 3. Geology 42, 1043-1046.
768   Mühlinghaus, C., Scholz, D., Mangini, A., 2009. Modelling fractionation of stable isotopes in
769   stalagmites. Geochimica et Cosmochimica Acta 73, 7275-7289.
770   Obert, J.C., Scholz, D., Felis, T., Brocas, W.M., Jochum, K.P., Andreae, M.O., 2016. 230Th/U
771   dating of Last Interglacial brain corals from Bonaire (southern Caribbean) using bulk and theca
772   wall material. Geochimica et Cosmochimica Acta 178, 20-40.
773   Pons-Branchu, E., Hamelin, B., Losson, B., Jaillet, S., Brulhet, J., 2010. Speleothem evidence
774   of warm episodes in northeast France during Marine Oxygen Isotope Stage 3 and implications
775   for permafrost distribution in northern Europe. Quaternary Research 74, 246-251.
776   Rasmussen, S.O., Bigler, M., Blockley, S.P., Blunier, T., Buchardt, S.L., Clausen, H.B.,
777   Cvijanovic, I., Dahl-Jensen, D., Johnsen, S.J., Fischer, H., 2014. A stratigraphic framework for
778   abrupt climatic changes during the Last Glacial period based on three synchronized Greenland
779   ice-core records: refining and extending the INTIMATE event stratigraphy. Quaternary Science
780   Reviews 106, 14-28.
781   Richards, D.A., Dorale, J.A., 2003. Uranium-series Chronology and Environmental
782   Applications of Speleothems. Reviews in Mineralogy and Geochemistry 52, 407.
783   Riechelmann, D.F.C., 2010. Aktuospeläologische Untersuchungen in der Bunkerhöhle des
784   Iserlohner Massenkalks (NRW/Deutschland): Signifikanz für kontinentale Klimaarchive. PhD,
785   Ruhr-Universität Bochum, Germany.
786   Riechelmann, D.F.C., Schröder-Ritzrau, A., Scholz, D., Fohlmeister, J., Spötl, C., Richter,
787   D.K., Mangini, A., 2011. Monitoring Bunker Cave (NW Germany): A prerequisite to interpret
788   geochemical proxy data of speleothems from this site. Journal of Hydrology 409, 682-695.
789   Riechelmann, D.F.C., Deininger, M., Scholz, D., Riechelmann, S., Schröder-Ritzrau, A., Spötl,
790   C., Richter, D.K., Mangini, A., Immenhauser, A., 2013. Disequilibrium carbon and oxygen
791   isotope fractionation in recent cave calcite: Comparison of cave precipitates and model data.
792   Geochimica et Cosmochimica Acta 103, 232-244.
793   Riechelmann, S., Buhl, D., Schröder-Ritzrau, A., Riechelmann, D.F.C., Richter, D.K., Vonhof,
794   H.B., Wassenburg, J.A., Geske, A., Spötl, C., Immenhauser, A., 2012a. The magnesium isotope
795   record of cave carbonate archives. Clim. Past 8, 1849-1867.
796   Riechelmann, S., Buhl, D., Schröder-Ritzrau, A., Spötl, C., Riechelmann, D.F.C., Richter,
797   D.K., Kluge, T., Marx, T., Immenhauser, A., 2012b. Hydrogeochemistry and fractionation
798   pathways of Mg isotopes in a continental weathering system: Lessons from field experiments.
799   Chemical Geology 300-301, 109-122.

Riechelmann, S., Schröder-Ritzrau, A., Wassenburg, J.A., Schreuer, J., Richter, D.K., Riechelmann, D.F.C., Terente, M., Constantin, S., Mangini, A., Immenhauser, A., 2014. Physicochemical characteristics of drip waters: Influence on mineralogy and crystal morphology of recent cave carbonate precipitates. Geochimica et Cosmochimica Acta 145, 13-29.

Riechelmann, S., Schröder-Ritzrau, A., Spötl, C., Riechelmann, D.F.C., Richter, D.K., Mangini, A., Frank, N., Breitenbach, S.F.M., Immenhauser, A., 2017. Sensitivity of Bunker Cave to climatic forcings highlighted through multi-annual monitoring of rain-, soil-, and dripwaters. Chemical Geology 449, 194-205.

Sánchez Goñi, M.F., Cacho, I., Turon, J.L., Guiot, J., Sierro, F.J., Peypouquet, J.P., Grimalt, J.O., Shackleton, N.J., 2002. Synchroneity between marine and terrestrial responses to millennial scale climatic variability during the last glacial period in the Mediterranean region. Climate dynamics 19, 95-105.

Sánchez Goñi, M.F., Bard, E., Landais, A., Rossignol, L., d'Errico, F., 2013. Air-sea temperature decoupling in western Europe during the last interglacial-glacial transition. Nature Geoscience 6, 837-841.

Scholz, D., Mangini, A., Felis, T., 2004. U-series dating of diagenetically altered fossil reef corals. Earth and Planetary Science Letters 218, 163-178.

Scholz, D., Hoffmann, D., 2008. 230Th/U-dating of fossil corals and speleothems. Quaternary Science Journal 57, 52–76.

Scholz, D., Mühlinghaus, C., Mangini, A., 2009. Modelling $\delta 13 C$ and $\delta 18 O$ in the solution layer on stalagmite surfaces. Geochimica et Cosmochimica Acta 73, 2592-2602.

Scholz, D., Hoffmann, D.L., 2011. StalAge–An algorithm designed for construction of speleothem age models. Quaternary Geochronology 6, 369-382.

Scholz, D., Frisia, S., Borsato, A., Spötl, C., Fohlmeister, J., Mudelsee, M., Miorandi, R., Mangini, A., 2012. Holocene climate variability in north-eastern Italy: potential influence of the NAO and solar activity recorded by speleothem data. Climate of the Past 8, 1367-1383.

Scholz, D., Tolzmann, J., Hoffmann, D.L., Jochum, K.P., Spötl, C., Riechelmann, D.F.C., 2014. Diagenesis of speleothems and its effect on the accuracy of 230Th/U-ages. Chemical Geology 387, 74-86.

Sirocko, F., Knapp, H., Dreher, F., Förster, M.W., Albert, J., Brunck, H., Veres, D., Dietrich, S., Zech, M., Hambach, U., Röhner, M., Rudert, S., Schwibus, K., Adams, C., Sigl, P., 2016. The ELSA-Vegetation-Stack: Reconstruction of Landscape Evolution Zones (LEZ) from laminated Eifel maar sediments of the last 60,000 years. Global and Planetary Change 142, 108-135.

Smart, P.L., Friedrich, H., 1987. Water movement and storage in the unsaturated zone of a maturely karstified aquifer, Mendip Hills, England. National Water Well Association, pp. 57-87.

Spötl, C., Mangini, A., 2002. Stalagmite from the Austrian Alps reveals Dansgaard–Oeschger events during isotope stage 3:: Implications for the absolute chronology of Greenland ice cores. Earth and Planetary Science Letters 203, 507-518.

Spötl, C., Mangini, A., Richards, D.A., 2006. Chronology and paleoenvironment of Marine Isotope Stage 3 from two high-elevation speleothems, Austrian Alps. Quaternary Science Reviews 25, 1127-1136.

Stewart, B.W., Capo, R.C., Chadwick, O.A., 1998. Quantitative strontium isotope models for weathering, pedogenesis and biogeochemical cycling. Geoderma 82, 173-195.

Svensson, A., Andersen, K.K., Bigler, M., Clausen, H.B., Dahl-Jensen, D., Davies, S.M., Johnsen, S.J., Muscheler, R., Parrenin, F., Rasmussen, S.O., 2008. A 60 000 year Greenland stratigraphic ice core chronology. Climate of the Past 4, 47-57.

Taylor, S.R., McLennan, S.M., McCulloch, M.T., 1983. Geochemistry of loess, continental crustal composition and crustal model ages. Geochimica et Cosmochimica Acta 47, 1897-1905.

851 Tooth, A.F., Fairchild, I.J., 2003. Soil and karst aquifer hydrological controls on the
852 geochemical evolution of speleothem-forming drip waters, Crag Cave, southwest Ireland.
853 Journal of Hydrology 273, 51-68.
854 Voelker, A.H.L., 2002. Global distribution of centennial-scale records for Marine Isotope Stage
855 (MIS) 3: a database. Quaternary Science Reviews 21, 1185-1212.
856 von Kamp, H., Ribbert, K.H., 2005. Erläuterungen zu Blatt 4611 Hagen-Hohenlimburg
857 Geologische Karte von Nordrhein-Westfalen 1: 25.000. Krefeld.
858 Wainer, K., Genty, D., Blamart, D., Hoffmann, D., Couchoud, I., 2009. A new stage 3
859 millennial climatic variability record from a SW France speleothem. Palaeogeography,
860 Palaeoclimatology, Palaeoecology 271, 130-139.
861 Wassenburg, J.A., Dietrich, S., Fietzke, J., Fohlmeister, J., Jochum, K.P., Scholz, D., Richter,
862 D.K., Sabaoui, A., Spotl, C., Lohmann, G., Andreae, M.O., Immenhauser, A., 2016.
863 Reorganization of the North Atlantic Oscillation during early Holocene deglaciation. Nature
864 Geoscience 9, 602-605.
865 Weber, M., Lugli, F., Jochum, K.P., Cipriani, A., Scholz, D., 2018. Calcium Carbonate and
866 Phosphate Reference Materials for Monitoring Bulk and Microanalytical Determination of Sr
867 Isotopes. Geostandards and Geoanalytical Research 42, 77-89.
868 Yang, Q., Scholz, D., Jochum, K.P., Hoffmann, D.L., Stoll, B., Weis, U., Schwager, B.,
869 Andreae, M.O., 2015. Lead isotope variability in speleothems—A promising new proxy for
870 hydrological change? First results from a stalagmite from western Germany. Chemical Geology
871 396, 143-151.
872 Zhou, H., Feng, Y.-x., Zhao, J.-x., Shen, C.-C., You, C.-F., Lin, Y., 2009. Deglacial variations
873 of Sr and ^{87}Sr/^{86}Sr ratio recorded by a stalagmite from Central China and their association with
874 past climate and environment. Chemical Geology 268, 233-247.

875